

# Climate stabilization by alkalinity production from pyrite burial during oceanic anoxia

Received: 9 May 2024

Accepted: 8 April 2025

Published online: 21 May 2025

 Check for updates

Mojtaba Fakhraee<sup>1,2,7</sup>✉, Kohen W. Bauer<sup>3,7</sup>✉, Noah J. Planavsky<sup>1</sup>, Christopher T. Reinhard<sup>4</sup> & Sean A. Crowe<sup>5,6</sup>✉

Pyrite formation and burial in anoxic ocean environments helps to regulate the acid–base balance of the oceans. Despite its potential importance, the impact of this anoxic alkalinity production on the global carbon cycle and Earth’s long-term climate regulation has been largely overlooked. Here, using a coupled carbon–sulfur cycle model, we show that pyrite burial could drive 5–46 Tmol yr<sup>-1</sup> of alkalinity production—up to about six times the modern background volcanic carbon flux—throughout the Phanerozoic eon. During periods of widespread oceanic anoxia (known as oceanic anoxic events), alkalinity production via pyrite burial is amplified and so becomes an important stabilizing mechanism for the climate system, counterbalancing carbon emissions from contemporaneous large igneous province volcanism. Our results indicate that the anoxia–alkalinity feedback was engaged during several of the most severe oceanic anoxic events from large igneous provinces during the past 300 Myr, and thus played a role in limiting the overall impacts of these events on the biosphere and climate. We conclude that ocean deoxygenation may provide an important negative feedback on ocean–atmosphere CO<sub>2</sub> partitioning, helping to buffer the impacts of CO<sub>2</sub> emission on the Earth system.

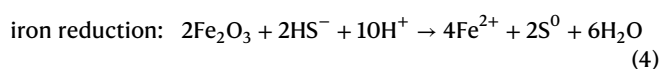
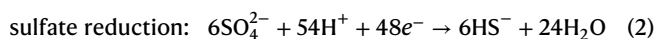
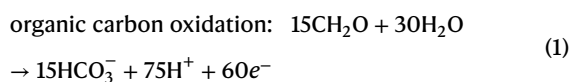
The global carbon cycle regulates atmospheric carbon dioxide (CO<sub>2</sub>) concentrations, exerting a major control on Earth’s climate and surface habitability. Atmospheric CO<sub>2</sub> concentrations are modulated by the magnitude of different input and output fluxes of CO<sub>2</sub> to the ocean–atmosphere system<sup>1,2</sup>. On geologic timescales (greater than 100 thousand years (kyr)), CO<sub>2</sub> inputs from volcanic emissions and oxidative organic carbon weathering on land are closely balanced by removal through the chemical weathering of carbonate and silicate rocks and the burial of carbonate minerals<sup>2</sup> and organic carbon in marine sediments<sup>3</sup>. Balance in the carbon cycle is maintained through long-term stabilizing feedbacks—foremost is the silicate weathering feedback,

wherein chemical weathering leads to the production of alkalinity at rates that depend on temperature and ambient CO<sub>2</sub> (refs. 4,5). Through interaction with the marine carbonate system, the production of alkalinity drives the precipitation and deposition of carbonate minerals and their removal through burial in marine sediments<sup>2</sup>, representing one of the main long-term sinks for CO<sub>2</sub> (ref. 6). Large-scale changes to ocean alkalinity budgets, for instance through shifts in the extent of marine clay production, can thus strongly impact atmospheric CO<sub>2</sub> concentrations with corresponding impacts on planetary climate<sup>7–9</sup>.

Ocean alkalinity is also produced during anaerobic respiration pathways in marine sediments. Most anaerobic alkalinity production

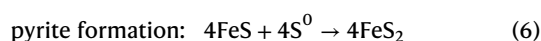
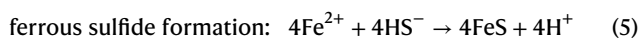
<sup>1</sup>Department of Earth and Planetary Sciences, Yale University, New Haven, CT, USA. <sup>2</sup>Department of Earth Sciences, University of Connecticut, Storrs, CT, USA. <sup>3</sup>Ocean Networks Canada, University of Victoria, Victoria, British Columbia, Canada. <sup>4</sup>School of Earth and Atmospheric Sciences, Georgia Institute of Technology, Atlanta, GA, USA. <sup>5</sup>Department of Earth Ocean and Atmospheric Science, University of British Columbia, Vancouver, British Columbia, Canada. <sup>6</sup>Department of Microbiology and Immunology, University of British Columbia, Vancouver, British Columbia, Canada. <sup>7</sup>These authors contributed equally: Mojtaba Fakhraee, Kohen W. Bauer. ✉e-mail: [mojtaba.fakhraee@yale.edu](mailto:mojtaba.fakhraee@yale.edu); [kohenbauer@gmail.com](mailto:kohenbauer@gmail.com); [sean.crowe@ubc.ca](mailto:sean.crowe@ubc.ca)

comes from sulfate reduction, which together with aerobic respiration, accounts for almost all organic carbon remineralization in marine sediments globally<sup>10,11</sup>. Notably, net alkalinity production from sulfate reduction only occurs when the sulfide produced during the process becomes buried as sedimentary pyrite<sup>12,13</sup>. Pyrite formation can be described by the following series of chemical half-reactions that illustrate the key stoichiometric relationships but are agnostic of the precise mechanisms of pyrite formation as these are varied, complex and remain the subject of debate<sup>14,15</sup>:

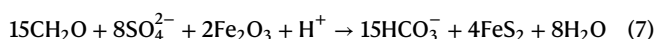


where  $\text{e}^-$  denotes electrons.

Assuming a two-step pyrite formation reaction<sup>16</sup>, these reactions drive downstream pyrite formation via:



Combining equations (1)–(6), we arrive at a net reaction that describes coupled sulfate and iron reduction that produces alkalinity and pyrite:



This net reaction yields two moles of alkalinity for each mole of sulfur reduced and buried as pyrite. By contrast, in the absence of pyrite formation the oxidation of sulfide produces acidity ( $\text{H}^+$ ) (the back reaction of equation (2)), which occurs at high rates in the oxygenated upper portions of the sediment column and consumes the alkalinity produced by sulfate reduction<sup>17</sup>. On the basis of equation (7), the ultimate formation of pyrite requires supplies of seawater sulfate and organic matter to fuel sulfate reduction, as well as highly reactive iron to form pyrite from the sulfide produced<sup>15</sup>. Current estimates of alkalinity production linked to pyrite burial in marine sediments are between 2.3 and 4.3 Tmol yr<sup>-1</sup>, or 4–7% of total global alkalinity production<sup>7,13</sup>. Whereas alkalinity delivered through the weathering of silicate and carbonate rocks is well-known as the primary sink for volcanic CO<sub>2</sub> (for example, see ref. 2), the impact of alkalinity production through pyrite burial on the regulation of Earth's surface CO<sub>2</sub> concentrations and climate has been largely overlooked<sup>18</sup>. Here we illustrate how alkalinity produced through pyrite burial likely had an important effect on atmospheric CO<sub>2</sub> concentrations throughout most of the Phanerozoic eon and show that it emerges as an important stabilizing feedback during intervals of elevated CO<sub>2</sub> emissions associated with expanded oceanic anoxia. The changing strength of this feedback likely contributed to varying climate sensitivities during different carbon-injection events<sup>19</sup>.

## Pyrite-driven alkalinity production during the Phanerozoic eon

Pyrite burial rates throughout the Phanerozoic eon can be used to estimate alkalinity generation through pyrite burial. Rates of pyrite burial during the Phanerozoic eon have been estimated on the basis

of sulfur isotope mass balances<sup>20–22</sup>, and in general these estimates indicate that pyrite was the dominant removal pathway for sulfur until about 350 million years ago (Ma), at which point sulfur buried as sulfate in evaporite minerals became the more important sink<sup>21</sup> (Fig. 1). Correspondingly, fluxes of alkalinity production can be estimated based on the stoichiometry of equation (7) by multiplying pyrite burial fluxes by a factor of two. Whereas reconstructions based on current knowledge of sulfur isotope ratios recorded in sulfate and pyrite remain incomplete and continue to evolve<sup>14</sup>, classical mass balance interpretations of sulfur isotope records suggest global pyrite-associated alkalinity production up to 6.5 Tmol yr<sup>-1</sup> during the Palaeozoic era, waning to approximately 2.0 Tmol yr<sup>-1</sup> by ~300 Ma and remaining approximately stable through to modern times (Fig. 1). Notably, our reconstructed pyrite-associated alkalinity fluxes for the last ~300 Ma converge on independent measurements for anoxic pyrite-driven alkalinity production in the modern ocean<sup>13</sup>, providing additional confidence in the reconstructions of the past. At a high level, these data illustrate that the strength of the pyrite-driven alkalinity production flux is linked to the fraction of marine sulfur exported as pyrite ( $f_{\text{pyrite}}$ ), indicating that intervals of elevated pyrite burial, such as during the Palaeozoic era (Fig. 1), have a stronger pyrite-driven buffering capacity on the atmospheric CO<sub>2</sub> concentration ( $p_{\text{CO}_2}$ ) and climate. Elevated pyrite burial during the Palaeozoic era, furthermore, is associated with widespread oceanic anoxia<sup>23</sup>. Oceanic anoxia channels water column respiration into anaerobic sulfate reduction<sup>24,25</sup>, which has the strong potential to promote sedimentary pyrite burial<sup>26</sup>. By analogy to ocean conditions during the Palaeozoic era, therefore, elevated pyrite burial also has strong potential for enhancing alkalinity production when anoxia is widespread.

Intermittent intervals of greatly expanded oceanic anoxia (known as oceanic anoxic events (OAEs)) developed beyond the Palaeozoic era, and these OAEs are commonly associated with massive CO<sub>2</sub> emissions from volcanism, climate catastrophe and ecological upheaval<sup>27,28</sup> (Fig. 1). Sulfate reduction associated with OAE intervals promotes sedimentary pyrite burial, and thus should also be associated with enhanced pyrite-driven alkalinity production fluxes<sup>29–31</sup>. Notably, ocean deoxygenation and enhanced pyrite burial associated with multiple OAEs has been linked to the drawdown of the seawater sulfate reservoir from 3–10 mM to <1 mM (refs. 32–35). Conservatively, such collapses in seawater sulfate concentrations are associated with—and partly driven by—increases in global pyrite burial rates by a factor of between two and five<sup>33,36–38</sup>. This translates to a commensurate increase in alkalinity fluxes driven by pyrite burial, corresponding to approximately 70–170% of the background volcanic carbon flux. As a result, alkalinity production through pyrite burial during intervals of expanded oceanic anoxia has enormous potential to offset enhanced CO<sub>2</sub> from associated large igneous province (LIP) volcanism.

## The oceanic anoxia–alkalinity feedback

To further evaluate the impact of ocean deoxygenation on pyrite burial rates and alkalinity production fluxes, we constructed a coupled carbon and sulfur mass balance model (Fig. 2). We explored the possible impact of oceanic anoxia on fluxes of pyrite-driven alkalinity production on the carbonic acid system by forcing the model from a steady state with an elevated volcanic CO<sub>2</sub> input. Initially, we modelled three generic end-member volcanic degassing scenarios to test the response of our model across a range of carbon-release events in terms of total magnitude and duration. We simulated three different scenarios corresponding to a total of  $1.7 \times 10^6$ ,  $4.2 \times 10^6$  and  $17 \times 10^6$  TmolC (approximately  $20 \times 10^3$ ,  $50 \times 10^3$  and  $205 \times 10^3$  PgC) emitted across 50, 500 and 1,000 kyr, respectively (Fig. 2a). These scenarios were chosen as a starting point to broadly contrast relatively small and rapid injection events with large and protracted events in the geologic record. Pyrite-associated alkalinity production fluxes were examined for all degassing scenarios across a range in the fraction of seafloor anoxia, varied from 0.1 to 20%,

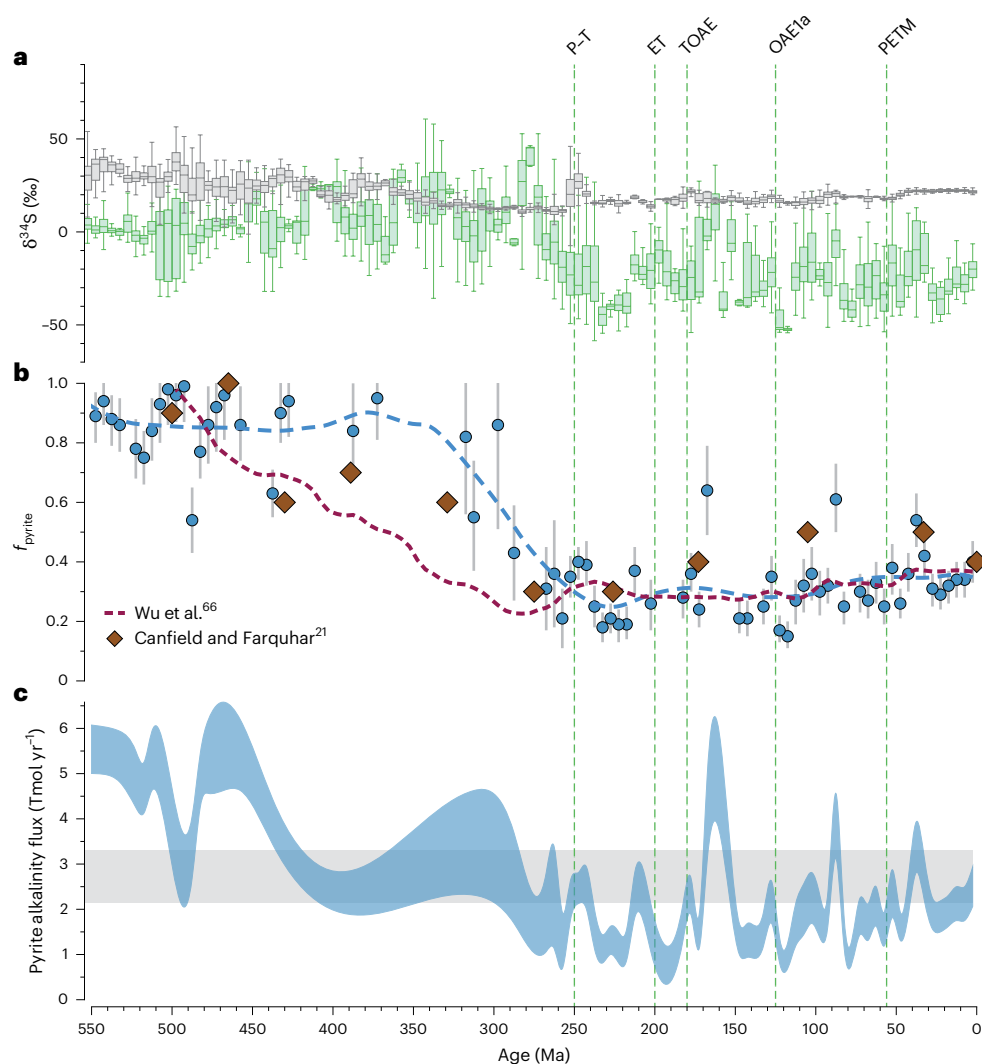


**Fig. 1 | Sulfur mass balance estimates of pyrite-driven alkalinity fluxes through Phanerozoic time.** **a**, Sulfate (grey boxes,  $n = 9,225$ ) and pyrite (green boxes,  $n = 7,752$ ) sulfur isotope ratio ( $\delta^{34}\text{S}$ ) values binned in intervals of 5 million years (Myr). The compiled  $\delta^{34}\text{S}$  data are from ref. 65. The IQR is the difference between the first and third quartiles. The whiskers are only drawn to the smallest/largest non-outlier. **b**, The fraction of sulfur buried as pyrite ( $f_{\text{pyrite}}$ ) as a function of time. We show different reconstructions of  $f_{\text{pyrite}}$  through time based on different sulfur isotope compilations<sup>21,66</sup>, including our own simple isotope mass balance estimate shown as blue circles, with the blue dashed line representing a LOESS

(locally estimated scatterplot smoothing) fit. The grey bars represent the maximum and minimum values based on the value of the oceanic input flux ( $F_{\text{input}}$ ) (Source Data Fig. 1). **c**, Smoothed (spline) alkalinity fluxes based on pyrite burial rates. The shading represents the minimum and maximum values based on  $F_{\text{input}}$ . The grey shading represents the range of the modern alkalinity flux based on pyrite burial<sup>213</sup>. The green dashed lines denote OAEs due to LIP volcanism in the past 300 Myr: Permian–Triassic mass extinction (P–T), end-Triassic mass extinction (ET), Toarcian Oceanic Anoxic Event (TOAE), oceanic anoxic event 1a (OAE1a) and the Palaeocene–Eocene Thermal Maximum (PETM).

as constrained by the likely expanse of oceanic anoxia during multiple Phanerozoic OAEs<sup>28</sup> (Fig. 2) (Supplementary Table 2). The impacts of oceanic anoxia and the alkalinity production fluxes from pyrite burial are reported as the difference ( $\Delta$ ) between model runs with and without the pyrite-associated alkalinity feedback.

The expansion of oceanic anoxia leads to enhanced pyrite burial and corresponding alkalinity fluxes which, in turn, offset enhanced  $p_{\text{CO}_2}$  from volcanism and effectively buffer oceanic pH. Our model confirms the sulfur isotope-based mass balance calculations (Fig. 1), with pyrite-burial-driven alkalinity fluxes of up to  $4 \text{ Tmol yr}^{-1}$  when oceanic anoxia is modern-like (0.1–0.5%)<sup>39</sup>. Notably, however, in contrast to the simple sulfur isotope mass balance calculations (Fig. 1), our more detailed biogeochemical model predicts appreciable increases in pyrite burial and corresponding alkalinity production during relatively short geologic intervals when volcanic  $\text{CO}_2$  input is strong, driving widespread anoxia and anoxia–alkalinity fluxes >20 times modern pyrite-associated alkalinity production fluxes<sup>7,13</sup> (Fig. 2).

Enhanced alkalinity production through ocean deoxygenation and pyrite burial thus provides a negative feedback on  $p_{\text{CO}_2}$ -driven climate warming, and can strongly impact the carbonic acid system, especially when both the volcanic  $\text{CO}_2$  input and the spatial extent of anoxia are appreciable.

The strength of the anoxia–alkalinity feedback on  $p_{\text{CO}_2}$  and pH scales with the extent of oceanic anoxia under both short and protracted volcanic degassing scenarios (Fig. 2). Under the low-emissions scenario ( $1.7 \times 10^6 \text{ TmolC}$  emitted over 50 kyr) with 10% seafloor anoxia, mean  $\Delta$ pyrite burial,  $\Delta p_{\text{CO}_2}$  and  $\Delta \text{pH}$  reach values of  $11.2 \text{ Tmol yr}^{-1}$ , 1,900 ppm and 0.5 pH units, respectively (Fig. 2). Under the high-emissions scenario ( $17 \times 10^6 \text{ TmolC}$  emitted over 1,000 kyr) with 10% seafloor anoxia,  $\Delta$ pyrite burial,  $\Delta p_{\text{CO}_2}$  and  $\Delta \text{pH}$  reach values of  $22 \text{ Tmol yr}^{-1}$ , 15,000 ppm, and 0.8 pH units, respectively (Fig. 2). Mechanistically, larger volcanic  $\text{CO}_2$  fluxes result in greater weathering-driven nutrient fluxes to the ocean, increasing marine productivity (see Methods). Increased marine productivity, in turn, drives elevated water

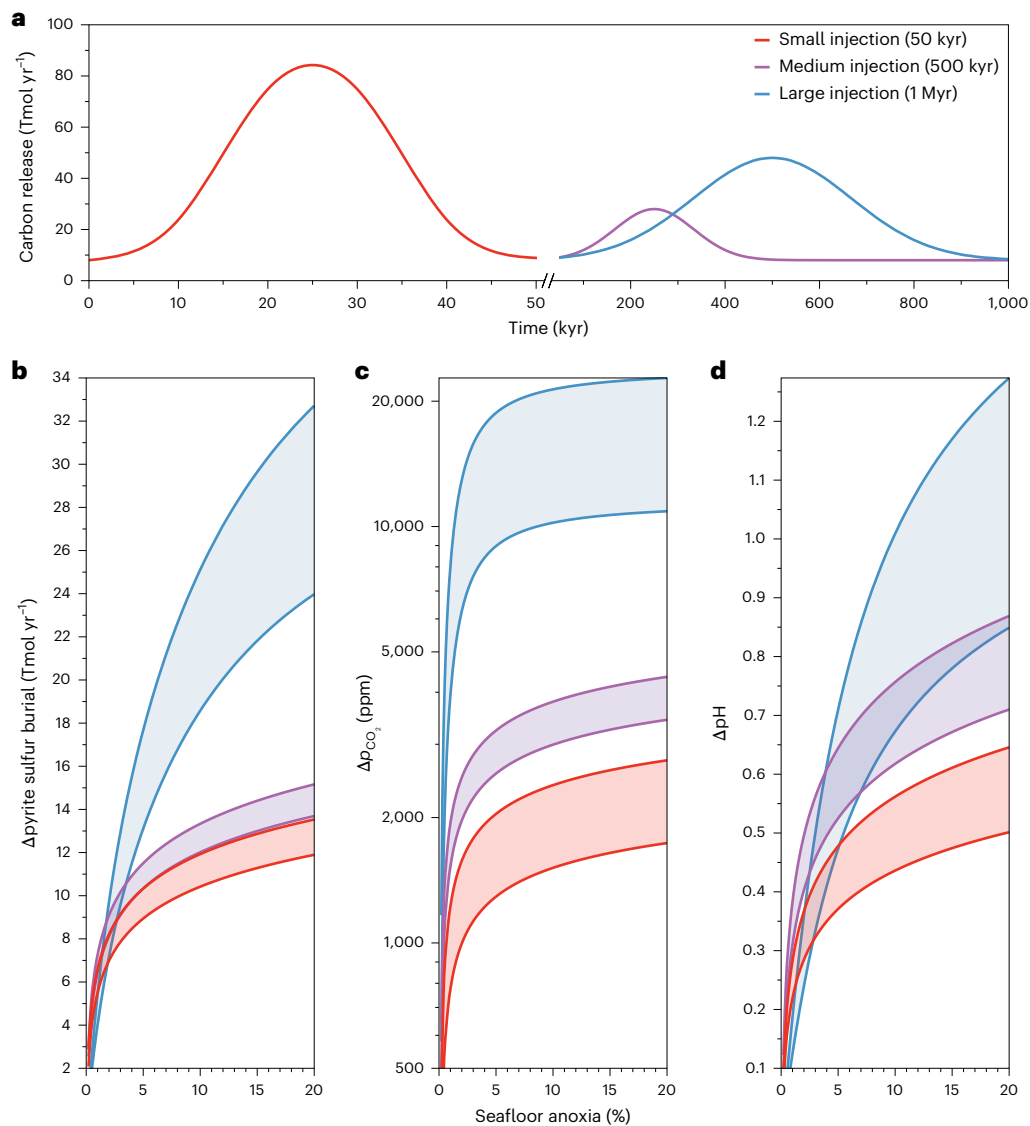


**Fig. 2 | Sensitivity of the coupled carbon and sulfur mass balance model.** **a**, Volcanic carbon-release scenarios used to drive the model. **b–d**, The change ( $\Delta$ ) in pyrite burial rate (**b**), atmospheric CO<sub>2</sub> (**c**) and ocean pH (**d**) as a function of oceanic anoxia for the volcanic degassing scenarios in **a**. The change data are

calculated as the difference between model runs with and without the anoxia–alkalinity feedback, with the shading representing  $\pm 50\%$  uncertainty on the degassing curves in **a**.

column oxygen demand and corresponding ocean deoxygenation. Under expanded anoxia, enhanced sulfate reduction and pyrite burial leads to the generation of alkalinity. Whereas these generic scenarios provide crucial sensitivity tests of our model, the spatial extent of oceanic anoxia in addition to the total magnitude and rate of volcanic CO<sub>2</sub> release varied greatly between specific oceanic anoxic events from large igneous provinces (LIP-OAEs) during the Phanerozoic eon<sup>19</sup>, which we explore in more detail below.

### Ocean-deoxygenation-produced alkalinity stabilizes climate

Many of the most severe OAEs are coeval with LIP events and volcanic CO<sub>2</sub> injection over the last 300 Myr of the Phanerozoic eon (Fig. 3a)<sup>27,40–42</sup>. Indeed, volcanism and associated climate warming is commonly cited as the ultimate driver of ocean deoxygenation, ecological upheaval and biological crises during OAEs<sup>43–45</sup>. We propose here that enhanced alkalinity production under expanded oceanic anoxia during OAEs acted as the key stabilizing feedback on climate during LIP CO<sub>2</sub> injection. We attempt to broadly constrain the strength of the anoxia–alkalinity feedback during multiple Phanerozoic LIP-OAEs (Fig. 3) by combining

published estimates for the spatial extent of oceanic anoxia<sup>19,28</sup> and volcanic CO<sub>2</sub> release<sup>27,40,42</sup> (Supplementary Table 2). On the basis of existing environmental reconstructions for five well-studied LIP-OAEs in the past 300 Myr, there is a strong positive correlation between the amount volcanic carbon degassing and the spatial extent of oceanic anoxia<sup>19</sup> (Fig. 3e). Acknowledging large uncertainties in the rate and timing of volcanic outgassing and evolution of oceanic redox conditions during these events, our models show that the anoxia–alkalinity feedback was particularly important during intervals associated with large volcanic CO<sub>2</sub> release and expansive oceanic anoxia (Fig. 3).

Our results indicate that alkalinity production in anoxic ocean regions may have played a role in limiting the overall impacts of LIP eruptions on the biosphere and climate system. For example, during the end-Triassic (ET), one of the five most severe biological crises of the Phanerozoic eon—volcanism from the emplacement of the Central Atlantic Magmatic Province (CAMP) LIP—initiated a biogeochemical cascade that included the deoxygenation of vast regions of global ocean that persisted for hundreds of thousands of years<sup>46,47</sup>. During the ET, our model predicts that anoxia-driven alkalinity production could have drawn peak atmospheric  $p_{\text{CO}_2}$  down by between

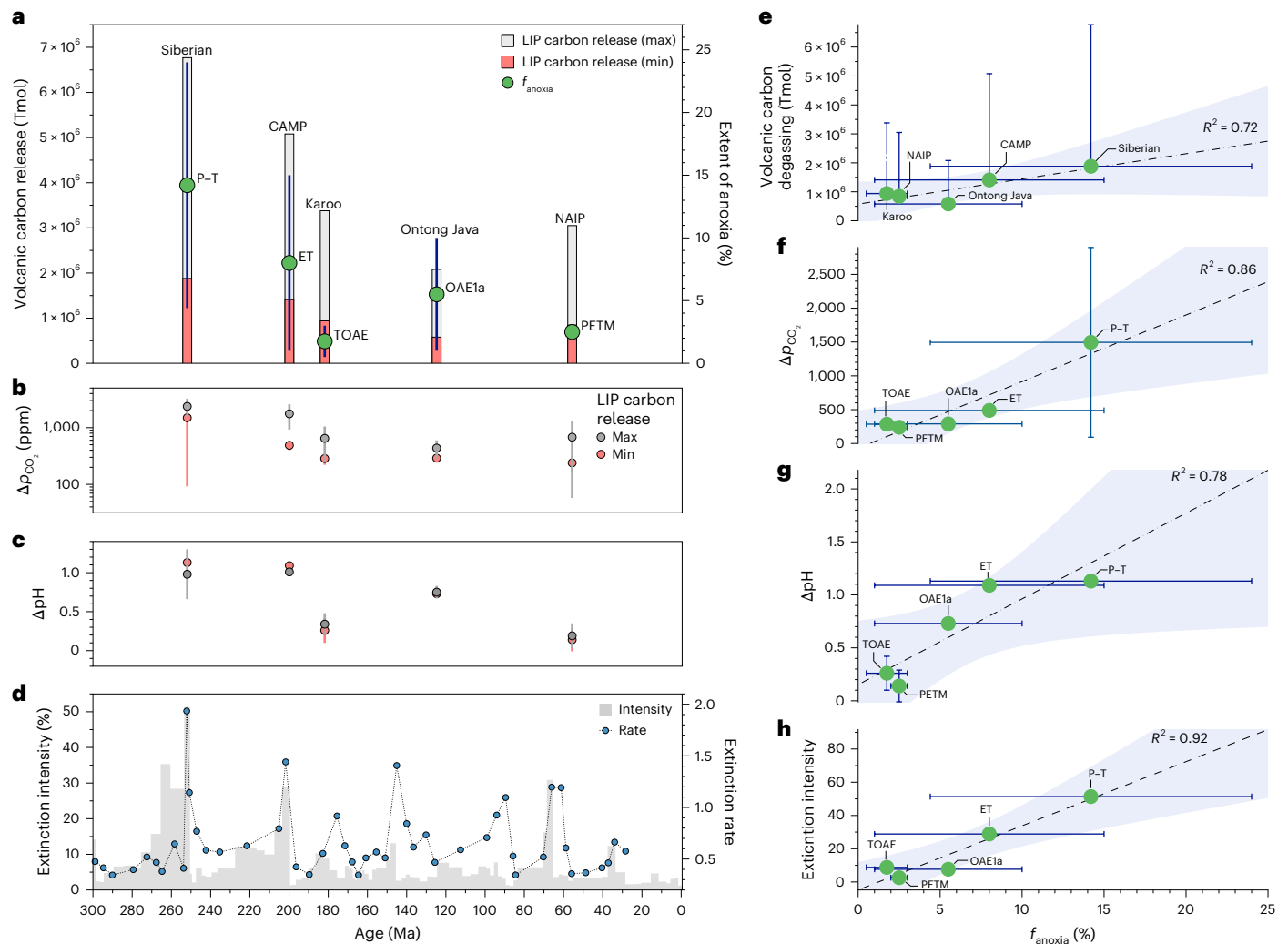


**Fig. 3 | The strength of the anoxia-alkalinity feedback during LIP-OAEs in the past 300 Myr.** **a**, LIP carbon release<sup>40,42</sup> and the severity of oceanic anoxia for different OAEs through time<sup>19,28</sup> (Supplementary Table 2). Modelled total carbon-release values (bars, left axis) correspond to estimates in Source Data Fig. 2. The green circles denote the average extent of anoxia ( $f_{\text{anoxia}}$ ; green circles, right axis), with the blue error bars representing the difference between the maximum and mean value (Source Data Fig. 2). The LIP-OAEs considered are as follows: the Siberian Traps eruption and the Permian–Triassic mass extinction (P–T); the Central Atlantic Magmatic Province (CAMP) eruption and the end-Triassic mass extinction (ET); the Karoo eruption and the Toarcian Oceanic Anoxic Event (TOAE); the Ontong Java Plateau eruption and Oceanic Anoxic Event 1a (OAE1a); and the North Atlantic Igneous Province (NAIP) eruption and the Palaeocene–Eocene Thermal Maximum (PETM). **b, c**, The modelled change in atmospheric

$\text{CO}_2$  (**b**) and ocean pH (**c**) for each LIP-OAE. Error bars extend to 1SD of model results based on model runs using both the upper and lower or maximum and minimum possible (**a**) volcanic carbon-emission rates for each event, with the circles representing the average value. **d**, Extinction intensity<sup>58</sup> (left axis) and rates<sup>27</sup> (right axis) through time. **e–h**, Different LIP-OAE characteristics versus the extent of OAE anoxia ( $f_{\text{anoxia}}$ ; percentage of total modern seafloor area) for volcanic carbon degassing (**e**), change in atmospheric  $\text{CO}_2$  (**f**), change in ocean pH (**g**) and extinction intensity (**h**). In all panels, model results for the lower degassing estimate from **a** are displayed. Error bars are the same as in **a–c**. In each panel a linear regression fit through the data is shown (dashed line), with the  $R^2$  value displayed, and where the shading represents the 95% confidence interval. **f** and **g** represent outputs from the model.  $R$ , coefficient of multiple correlation.

490 and 1,755 ppm and buffered ocean pH by between 1.01 and 1.09 units, depending on the volcanic carbon-delivery rates and the spatial extent of seafloor anoxia (Fig. 3). Notably, the pyrite burial rates predicted by our model are broadly consistent with independent proxy evidence and numerical models that suggest greatly enhanced pyrite burial fluxes under widespread anoxia during this time<sup>33</sup>. Although absolute  $p_{\text{CO}_2}$  estimates for the ET event vary between proxies, stable carbon isotopes in pedogenic carbonates suggest a maximum  $p_{\text{CO}_2}$  increase of  $2,200 \pm 1,000$  ppm (ref. 48).

Conservatively, comparing our minimum model-based estimates for  $\Delta p_{\text{CO}_2}$  with the reconstructed change based on proxy evidence suggests that the anoxia-alkalinity feedback could have limited  $p_{\text{CO}_2}$  increase by at least 15–22% relative to the hypothetical scenario without the feedback, indicating that pyrite burial and anoxia-associated alka-

linity played a quantitatively important role in stabilizing the climate during the event. In addition, there is geological and palaeontological evidence for a biocalcification crisis during the ET event<sup>49</sup> in both shelf<sup>50</sup> and deep-water settings<sup>51</sup>. However, estimates for the absolute decline in ocean pH are lacking, making it difficult to quantify how seawater buffering through pyrite-associated alkalinity production may have limited ocean acidification. Nonetheless, given the relationships between the amount of carbon injection, the magnitude of the anoxia-alkalinity feedback and the severity of extinction (Fig. 3), our results indicate that the anoxia-alkalinity feedback probably played an important role in mitigating further biological collapse through buffering of ocean acidity and limiting climate warming.

Despite a scaling between the magnitude of volcanic degassing and the extent of oceanic anoxia (Fig. 2), the anoxia-alkalinity feedback

appears to have had a more limited relative capacity to mitigate ecological upheaval during the Permian–Triassic mass extinction (P–T), the most severe mass extinction in Earth’s history<sup>52</sup> (Fig. 3). During the P–T boundary event, our model predicts pyrite-driven alkalinity production could have drawn atmospheric  $p_{\text{CO}_2}$  down by between 1,500 and 2,370 ppm and buffered ocean pH by an average  $1.05 \pm 0.32$  units (Fig. 3). Furthermore, acknowledging that the temporal fabric of volcanic degassing and seawater redox evolution across the P–T boundary (and other LIP-OAEs studied herein) was probably more complex than represented in our model (for example, by a Gaussian distribution), our results do show reasonable consistency with key environmental reconstructions based on available proxy evidence, both in terms of the relative magnitude and timing of environmental perturbations, indicating that the anoxia–alkalinity feedback was active (Supplementary Fig. 1). Indeed, despite the strong engagement of anoxia–alkalinity feedback, geochemical proxy evidence and numerical models both suggest dramatic and sustained changes in  $p_{\text{CO}_2}$  and pH<sup>53,54</sup> as well as in temperature<sup>55,56</sup>, which suppressed ecosystem recovery for millions of years following forcing. A breakdown of Earth’s critical stabilizing feedbacks across the P–T has been explained by the extreme quantity and rate of CO<sub>2</sub> emissions, which may have exhausted the capacity of multiple Earth system processes, including silicate weathering, marine clay formation<sup>54</sup> and the anoxia–alkalinity feedbacks, to effectively buffer the climate<sup>57</sup>.

Nonetheless, our model results are in agreement with previous observations which suggest that, compared with very massive carbon injections—such as the P–T event—that have the potential to overwhelm the total buffering capacity of the Earth’s main stabilizing feedbacks, smaller carbon injections (for example, the Toarcian OAE or the Palaeocene–Eocene Thermal Maximum) are associated with relatively rapid climate recovery, more limited temperature swings and less severe biological impacts<sup>27,58</sup> (Fig. 3). This implies a critical threshold linked to the magnitude and rate of carbon injection that once traversed exhausts the ability of key negative feedbacks in the Phanerozoic carbon cycle—including the anoxia–alkalinity feedback—to effectively stabilize climate and ocean chemistry. Links between the extent of deoxygenation and reactive-iron-limited pyrite burial may play a key role in controlling this threshold. However, additional physicochemical, biological and tectonic influences<sup>54,57</sup>, such as the intensity of reverse weathering<sup>54</sup>, sediment diagenesis<sup>59</sup>, ocean circulation<sup>60</sup> and continental configuration<sup>61</sup>, probably also shape the strength of the feedback. This hypothesis can be further tested in Earth system, mass balance and diagenetic models that include the anoxia–alkalinity feedback in future efforts to further constrain past carbon cycling and climate variability.

Whereas the anoxia–alkalinity feedback increases the oceanic CO<sub>2</sub> sink on timescales of LIP-OAE initiation and recovery, enhanced pyrite and organic carbon burial during these events may ultimately provide a source of CO<sub>2</sub> on much longer timescales. Enhanced pyrite and organic carbon burial during LIP-OAEs generates a larger sedimentary reservoir of reduced equivalents with potential for tectonically driven recycling in the Earth’s crust. For example, if ultimately exposed at the continent surface, pyrite would drive greater acid generation as the result of oxidative weathering<sup>62</sup>. Dissolution of carbonate minerals with the acid produced results in the transfer of sedimentary carbon into the ocean–atmosphere system as CO<sub>2</sub> (ref. 63). Sulfide oxidation and carbonate dissolution as a source of CO<sub>2</sub> have been proposed as an important stabilizing feedback on climate throughout the Cenozoic era, when denudation and corresponding silicate weathering rates were high and volcanic CO<sub>2</sub> emissions were relatively low<sup>63</sup>. As a succession of LIP-OAEs associated with enhanced pyrite burial occurred in a relatively short time frame during the Mesozoic era (Fig. 3)<sup>64</sup>, we hypothesize that integrated pyrite burial during these events may have primed the crustal reservoir of reduced sulfur and thus possibly played a role in subsequent Cenozoic climate regulation through sulfide

oxidation across the following 65 Myr (ref. 63). Such a mechanistic explanation would depend on the complex interplay between rates of crustal recycling and redistribution as well as sea-level change, among other factors<sup>61</sup>.

The relationships between pyrite burial, anoxic alkalinity production, ocean chemistry and climate during some of the most significant environmental perturbations during the Phanerozoic eon may provide historical context for the potential impacts of contemporary climate warming and ocean deoxygenation. By analogy to the climatic anomalies and OAEs of the past 300 Myr, if modern carbon emissions and ocean deoxygenation drive similar Earth system responses, the expansion of oceanic anoxia and the corresponding production of alkalinity may once again emerge as an important stabilizing feedback on ocean chemistry and Earth’s climate.

## Online content

Any methods, additional references, Nature Portfolio reporting summaries, source data, extended data, supplementary information, acknowledgements, peer review information; details of author contributions and competing interests; and statements of data and code availability are available at <https://doi.org/10.1038/s41561-025-01698-0>.

## References

1. Kump, L. R. & Garrels, R. M. Modeling atmospheric O<sub>2</sub> in the global sedimentary redox cycle. *Am. J. Sci.* **286**, 337–360 (1986).
2. Berner, R. A., Lasaga, A. C. & Garrels, R. M. Carbonate-silicate geochemical cycle and its effect on atmospheric carbon dioxide over the past 100 million years. *Am. J. Sci.* **283**, 641–683 (1983).
3. Berner, R. A. & Raiswell, R. Burial of organic carbon and pyrite sulfur in sediments over Phanerozoic time: a new theory. *Geochim. Cosmochim. Acta* **47**, 855–862 (1983).
4. Zeebe, R. E. & Caldeira, K. Close mass balance of long-term carbon fluxes from ice-core CO<sub>2</sub> and ocean chemistry records. *Nat. Geosci.* **1**, 312–315 (2008).
5. Walker, J. C. G., Hays, P. B. & Kasting, J. F. A negative feedback mechanism for the long-term stabilization of Earth’s surface temperature. *J. Geophys. Res. Oceans* **86**, 9776–9782 (1981).
6. Berner, R. A. *The Phanerozoic Carbon Cycle: CO<sub>2</sub> and O<sub>2</sub>* (Oxford Univ. Press, 2004).
7. Middelburg, J. J., Soetaert, K. & Hagens, M. Ocean alkalinity, buffering and biogeochemical processes. *Rev. Geophys.* **58**, e2019RG000681 (2020).
8. Isson, T. T. et al. Evolution of the global carbon cycle and climate regulation on earth. *Global Biogeochem. Cycles* **34**, e2018GB006061 (2020).
9. Torres, M. A., Moosdorf, N., Hartmann, J., Adkins, J. F. & West, A. J. Glacial weathering, sulfide oxidation, and global carbon cycle feedbacks. *Proc. Natl Acad. Sci. USA* **114**, 8716–8721 (2017).
10. Jørgensen, B. B. Mineralization of organic matter in the sea bed—the role of sulphate reduction. *Nature* **296**, 643–645 (1982).
11. Canfield, D. E. Organic matter oxidation in marine sediments. In *Interactions of C, N, P and S Biogeochemical Cycles and Global Change* (eds Wollast, R. et al.) 333–363 (Springer, 1993).
12. Mucci, A. et al. The fate of carbon in continental shelf sediments of eastern Canada: a case study. *Deep Sea Res. 2 Top. Stud. Oceanogr.* **47**, 733–760 (2000).
13. Hu, X. & Cai, W.-J. An assessment of ocean margin anaerobic processes on oceanic alkalinity budget. *Global Biogeochem. Cycles* <https://doi.org/10.1029/2010GB003859> (2011).
14. Bryant, R. N. et al. Deconvolving microbial and environmental controls on marine sedimentary pyrite sulfur isotope ratios. *Science* **382**, 912–915 (2023).
15. Berner, R. A. Sedimentary pyrite formation: an update. *Geochim. Cosmochim. Acta* **48**, 605–615 (1984).

16. Berner, R. A. Sedimentary pyrite formation. *Am. J. Sci.* **268**, 1–23 (1970).
17. Reithmaier, G. M. S. et al. Alkalinity production coupled to pyrite formation represents an unaccounted blue carbon sink. *Global Biogeochem. Cycles* **35**, e2020GB006785 (2021).
18. Reinhard, C. T. & Fischer, W. W. Mechanistic links between the sedimentary redox cycle and marine acid–base chemistry. *Geochem. Geophys. Geosyst.* **20**, 5968–5978 (2019).
19. Chen, J. et al. Marine anoxia linked to abrupt global warming during Earth’s penultimate icehouse. *Proc. Natl Acad. Sci. USA* **119**, e2115231119 (2022).
20. Halevy, I., Peters, S. E. & Fischer, W. W. Sulfate burial constraints on the Phanerozoic sulfur cycle. *Science* **337**, 331–334 (2012).
21. Canfield, D. E. & Farquhar, J. Animal evolution, bioturbation, and the sulfate concentration of the oceans. *Proc. Natl Acad. Sci. USA* **106**, 8123–8127 (2009).
22. Canfield, D. E. Sulfur isotopes in coal constrain the evolution of the Phanerozoic sulfur cycle. *Proc. Natl Acad. Sci. USA* **110**, 8443–8446 (2013).
23. Sperling, E. A. et al. A long-term record of early to mid-Paleozoic marine redox change. *Sci. Adv.* **7**, eabf4382 (2021).
24. Hastings, D. & Emerson, S. Sulfate reduction in the presence of low oxygen levels in the water column of the Cariaco Trench. *Limnol. Oceanogr.* **33**, 391–396 (1988).
25. Callbeck, C. M. et al. Sulfur cycling in oceanic oxygen minimum zones. *Limnol. Oceanogr.* **66**, 2360–2392 (2021).
26. Fakhraee, M., Crowe, S. A. & Katsev, S. Sedimentary sulfur isotopes and Neoproterozoic ocean oxygenation. *Sci. Adv.* **4**, e1701835 (2018).
27. Clapham, M. E. & Renne, P. R. Flood basalts and mass extinctions. *Annu. Rev. Earth Planet. Sci.* **47**, 275–303 (2019).
28. Reershemius, T. & Planavsky, N. J. What controls the duration and intensity of ocean anoxic events in the Paleozoic and the Mesozoic? *Earth Sci. Rev.* **221**, 103787 (2021).
29. Bauer, K. W. et al. Ferruginous oceans during OAE1a and collapse of the marine sulfate pool. *Earth Planet. Sci. Lett.* **578**, 117324 (2022).
30. Berner, R. A. Burial of organic carbon and pyrite sulfur in the modern ocean: its geochemical and environmental significance. *Am. J. Sci.* **282**, 451–473 (1982).
31. Fakhraee, M., Hancisse, O., Canfield, D. E., Crowe, S. A. & Katsev, S. Proterozoic seawater sulfate scarcity and the evolution of ocean–atmosphere chemistry. *Nat. Geosci.* **12**, 375–380 (2019).
32. Fakhraee, M., Bauer, K. W. & Crowe, S. A. Seawater sulfate dynamics and a new tipping point in the Earth system. *Geology* **52**, 906–910 (2024).
33. He, T. et al. An enormous sulfur isotope excursion indicates marine anoxia during the end-Triassic mass extinction. *Sci. Adv.* **6**, eabb6704 (2020).
34. Cai, C., Xu, C., Fakhraee, M., Chen, D. & Peng, Y. Significant fluctuation in the global sulfate reservoir and oceanic redox state during the Late Devonian event. *PNAS Nexus* **1**, pgac122 (2022).
35. Schobben, M. et al. Volatile earliest Triassic sulfur cycle: a consequence of persistent low seawater sulfate concentrations and a high sulfur cycle turnover rate? *Palaeogeogr. Palaeoclimatol. Palaeoecol.* **486**, 74–85 (2017).
36. Yao, W., Paytan, A. & Wortmann, U. G. Large-scale ocean deoxygenation during the Paleocene–Eocene Thermal Maximum. *Science* **361**, 804–806 (2018).
37. Gomes, M. L. & Hurtgen, M. T. Sulfur isotope fractionation in modern euxinic systems: implications for paleoenvironmental reconstructions of paired sulfate–sulfide isotope records. *Geochim. Cosmochim. Acta* **157**, 39–55 (2015).
38. Salisbury, J. et al. An 80-million-year sulphur isotope record of pyrite burial over the Permian–Triassic. *Sci. Rep.* **12**, 17370 (2022).
39. Remírez, M. N. et al. Carbonate uranium isotopes record global expansion of marine anoxia during the Toarcian Oceanic Anoxic Event. *Proc. Natl Acad. Sci. USA* **121**, e2406032121 (2024).
40. Jiang, Q., Jourdan, F., Olierook, H. K. H. & Merle, R. E. An appraisal of the ages of Phanerozoic large igneous provinces. *Earth Sci. Rev.* **237**, 104314 (2023).
41. Penn, J. L. & Deutsch, C. Avoiding ocean mass extinction from climate warming. *Science* **376**, 524–526 (2022).
42. Jiang, Q. et al. Volume and rate of volcanic CO<sub>2</sub> emissions governed the severity of past environmental crises. *Proc. Natl Acad. Sci. USA* **119**, e2202039119 (2022).
43. Jenkyns, H. C. Geochemistry of oceanic anoxic events. *Geochem. Geophys. Geosyst.* <https://doi.org/10.1029/2009GC002788> (2010).
44. Adams, D. D., Hurtgen, M. T. & Sageman, B. B. Volcanic triggering of a biogeochemical cascade during Oceanic Anoxic Event 2. *Nat. Geosci.* **3**, 201–204 (2010).
45. Bottini, C., Cohen, A. S., Erba, E., Jenkyns, H. C. & Coe, A. L. Osmium-isotope evidence for volcanism, weathering, and ocean mixing during the early Aptian OAE 1a. *Geology* **40**, 583–586 (2012).
46. Somlyay, A. et al. Uranium isotope evidence for extensive seafloor anoxia after the end-Triassic mass extinction. *Earth Planet. Sci. Lett.* **614**, 118190 (2023).
47. He, T. et al. Extensive marine anoxia in the European epicontinental sea during the end-Triassic mass extinction. *Glob. Planet. Change* **210**, 103771 (2022).
48. Schaller, M. F., Wright, J. D. & Kent, D. V. Atmospheric P<sub>CO<sub>2</sub></sub> perturbations associated with the Central Atlantic Magmatic Province. *Science* **331**, 1404–1409 (2011).
49. Kiessling, W. & Simpson, C. On the potential for ocean acidification to be a general cause of ancient reef crises. *Glob. Change Biol.* **17**, 56–67 (2011).
50. Črne, A. E., Weissert, H., Goričan, Š. & Bernasconi, S. M. A biocalcification crisis at the Triassic–Jurassic boundary recorded in the Budva Basin (Dinarides, Montenegro). *Geol. Soc. Am. Bull.* **123**, 40–50 (2011).
51. Ikeda, M., Hori, R. S., Okada, Y. & Nakada, R. Volcanism and deep-ocean acidification across the end-Triassic extinction event. *Palaeogeogr. Palaeoclimatol. Palaeoecol.* **440**, 725–733 (2015).
52. Dal Corso, J. et al. Environmental crises at the Permian–Triassic mass extinction. *Nat. Rev. Earth Environ.* **3**, 197–214 (2022).
53. Jurikova, H. et al. Permian–Triassic mass extinction pulses driven by major marine carbon cycle perturbations. *Nat. Geosci.* **13**, 745–750 (2020).
54. Isson, T. T. et al. Marine siliceous ecosystem decline led to sustained anomalous Early Triassic warmth. *Nat. Commun.* **13**, 3509 (2022).
55. Sun, Y. et al. Lethally hot temperatures during the Early Triassic greenhouse. *Science* **338**, 366–370 (2012).
56. Joachimski, M. M. et al. Climate warming in the latest Permian and the Permian–Triassic mass extinction. *Geology* **40**, 195–198 (2012).
57. Kump, L. R. Prolonged Late Permian–Early Triassic hyperthermal: failure of climate regulation? *Philos. Trans. R. Soc. Lond. A* **376**, 20170078 (2018).
58. Rohde, R. A. & Muller, R. A. Cycles in fossil diversity. *Nature* **434**, 208–210 (2005).
59. Berelson, W. et al. A time series of benthic flux measurements from Monterey Bay, CA. *Cont. Shelf Res.* **23**, 457–481 (2003).
60. Ge, Y. & Bond, D. P. G. Two deep marine oxygenation events during the Permian–Triassic boundary interval in South China: relationship with ocean circulation and marine primary productivity. *Earth Sci. Rev.* **234**, 104220 (2022).
61. Pohl, A. et al. Continental configuration controls ocean oxygenation during the Phanerozoic. *Nature* **608**, 523–527 (2022).

62. Berner, R. A. GEOCARBSULF: a combined model for Phanerozoic atmospheric O<sub>2</sub> and CO<sub>2</sub>. *Geochim. Cosmochim. Acta* **70**, 5653–5664 (2006).
63. Torres, M. A., West, A. J. & Li, G. Sulphide oxidation and carbonate dissolution as a source of CO<sub>2</sub> over geological timescales. *Nature* **507**, 346 (2014).
64. Emmings, J. F. et al. Pyrite mega-analysis reveals modes of anoxia through geological time. *Sci. Adv.* **8**, eabj5687 (2022).
65. Fakhraee, M. et al. The history of Earth's sulfur cycle. *Nat. Rev. Earth Environ.* **6**, 106–125 (2025).
66. Wu, N., Farquhar, J., Strauss, H., Kim, S.-T. & Canfield, D. E. Evaluating the S-isotope fractionation associated with Phanerozoic pyrite burial. *Geochim. Cosmochim. Acta* **74**, 2053–2071 (2010).

**Publisher's note** Springer Nature remains neutral with regard to jurisdictional claims in published maps and institutional affiliations.

Springer Nature or its licensor (e.g. a society or other partner) holds exclusive rights to this article under a publishing agreement with the author(s) or other rightsholder(s); author self-archiving of the accepted manuscript version of this article is solely governed by the terms of such publishing agreement and applicable law.

© The Author(s), under exclusive licence to Springer Nature Limited 2025

## Methods

### Global carbon and sulfur mass balance model

To explore the impact of anoxia and pyrite burial on the global carbon cycle, we used the following simple formulations that couple sulfur and carbon cycling in the ocean–atmosphere system. The carbon mass balance equations account for changes in marine dissolved inorganic carbon (DIC), total alkalinity (TA), and atmospheric CO<sub>2</sub> ( $p_{\text{CO}_2}$ ):

$$\frac{d\text{DIC}}{dt} = J_{\text{carb,weath}} + J_{\text{silic,weath}} - J_{\text{NPP}} - 0.5 \times J_{\text{carb,auth}} - 0.5 \times J_{\text{carb,bio}} - J_{\text{air,sea}} \quad (8)$$

$$\frac{d\text{TA}}{dt} = J_{\text{carb,weath}} + J_{\text{silic,weath}} + J_{\text{silic,mar}} + 2 \times J_{\text{pyr}} - J_{\text{carb,auth}} - J_{\text{carb,bio}} - J_{\text{silic,mar,rev}} \quad (9)$$

$$\frac{dp_{\text{CO}_2}}{dt} = J_{\text{air,sea}} + J_{\text{org,weath}} + J_{\text{degass}} - 0.5 \times J_{\text{carb,weath}} - J_{\text{silic,weath}} \quad (10)$$

$$\frac{d[\text{SO}_4^{2-}]}{dt} = J_{\text{sulfur,weath}} + J_{\text{sulfur,volc}} - J_{\text{gyp}} - J_{\text{pyr}} \quad (11)$$

where equations (8)–(10) and (11) represent changes in the concentration of different carbon species and sulfate, respectively, with time  $t$ . The variables  $J$  denote the fluxes of the species involved, and parameterization of the different sources and sinks of the different species is detailed below.  $J_{\text{silic,mar,rev}}$  is the rate of reverse silicate weathering in marine system.  $J_{\text{degass}}$  is the flux of volcanic CO<sub>2</sub> degassing.  $J_{\text{sulfur,weath}}$  is the rate of sulfur weathering.  $J_{\text{sulfur,volc}}$  is the flux of sulfur degassing. The model pH is calculated from the DIC and TA concentrations using a built-in function in MATLAB that calculates the different species in the carbonic acid system (for example, pH, [CO<sub>3</sub><sup>2-</sup>]) from two known species, in this case, DIC and TA<sup>67</sup>.

$J_{\text{carb,weath}}$  and  $J_{\text{silic,weath}}$ . The fluxes of carbonate and silicate weathering ( $J_{\text{carb,weath}}$  and  $J_{\text{silic,weath}}$ , respectively) were parameterized using previous studies<sup>68</sup>:

$$J_{\text{carb,weath}} = J_{\text{carb,weath,mod}} \left( \frac{p_{\text{CO}_2}}{p_{\text{CO}_2,\text{mod}}} \right)^{\alpha_1} \quad (12)$$

$$J_{\text{silic,weath}} = J_{\text{silic,weath,mod}} \left( \frac{p_{\text{CO}_2}}{p_{\text{CO}_2,\text{mod}}} \right)^{\alpha_2} \quad (13)$$

Here,  $J_{\text{carb,weath,mod}}$ ,  $J_{\text{silic,weath,mod}}$  and  $p_{\text{CO}_2,\text{mod}}$  are the modern values for carbonate and silicate weathering fluxes and the atmospheric CO<sub>2</sub> concentration, respectively. The coefficients  $\alpha_1$  and  $\alpha_2$  denote the strength of the response of carbonate and silicate weathering to the change in  $p_{\text{CO}_2}$ , respectively, and their values were used from previous studies<sup>68</sup>.  $J_{\text{silic,mar}}$ , the flux of silicate buried in marine sediment, is also considered to follow the same parameterization as  $J_{\text{silic,weath}}$ , where the concentration of  $p_{\text{CO}_2}$  in the water is calculated using the concentrations of DIC and TA.

$J_{\text{NPP}}$ . The flux of carbon burial in the ocean ( $J_{\text{NPP}}$ ) can be parameterized as:

$$J_{\text{NPP}} = \varepsilon \times \text{NPP} \times (f_{\text{oxic}} \times \text{area}), \quad (14)$$

where  $\varepsilon$  is the efficiency of the carbon pump, NPP is the strength of marine net primary production and the final term denotes the area of the ocean (area) corrected for the fraction of oxic ocean in which oxygen production occurs ( $f_{\text{oxic}}$ ). Similar to previous work, the value of NPP can be related to the modern NPP ( $\text{NPP}_{\text{mod}}$ ) and the strength of

the silicate weathering flux that reflects the effect of nutrient delivery to the ocean as follows<sup>69,70</sup>:

$$\text{NPP} = \text{NPP}_{\text{mod}} \times \left( \frac{J_{\text{silic,weath}}}{J_{\text{silic,weath,mod}}} \right). \quad (15)$$

This relationship is based on the assumption of the steady-state global phosphorus mass balance. The burial efficiency of a point in time with different anoxic area fractions can also be calculated as:

$$\varepsilon = f_{\text{anoxia}} \times \varepsilon_{\text{anoxic}} + f_{\text{oxic}} \times \varepsilon_{\text{oxic}}, \quad (16)$$

where the parameters  $f_{\text{anoxia}}$ ,  $\varepsilon_{\text{anoxic}}$ ,  $f_{\text{oxic}}$  and  $\varepsilon_{\text{oxic}}$  are the fraction of anoxia in the ocean, the efficiency of the carbon pump under anoxic conditions, the areal fraction of oxic conditions in the ocean and the efficiency of the carbon pump under oxic (modern) conditions. We used a high burial efficiency under anoxic conditions, consistent with modelling and experimental results<sup>71,72</sup> and the modern observations that indicate an increase in the burial efficiency of carbon under anoxic conditions. The fraction of oxic conditions is calculated as the remainder relative to anoxic conditions.

$J_{\text{carb,auth}}$  and  $J_{\text{carb,bio}}$ . The fluxes of authigenic and biogenic carbonate ( $J_{\text{carb,auth}}$  and  $J_{\text{carb,bio}}$ , respectively) were parameterized as a function of the calcium carbonate saturation state and the strength of marine net primary production (NPP):

$$J_{\text{carb,auth}} = k_{\text{CaCO}_3} \times (\Omega - 1)^\eta \quad (17)$$

$$J_{\text{carb,bio}} = \text{NPP} \times \alpha_{\text{rain}}, \quad (18)$$

where  $k_{\text{CaCO}_3}$ ,  $\Omega$  and  $\eta$  are the rate constant for calcium carbonate precipitation, the calcium carbonate saturation state and the reaction order for calcium carbonate precipitation, respectively. The saturation state was calculated using the equilibrium constant for calcium carbonate precipitation and concentrations of calcium ([Ca<sup>2+</sup>]) and carbonate ([CO<sub>3</sub><sup>2-</sup>]) ions<sup>67</sup>. The concentration of calcium is set to be constant at the modern value (-10 mM) and the concentration of carbonate was calculated from concentrations of DIC and TA using a built-in function that calculates the different species in the carbonic acid system from two known species.

The coefficient  $\alpha_{\text{rain}}$  corresponds to the rain ratio, which is the ratio of calcium carbonate to organic matter in marine particles (CaCO<sub>3</sub>:POC).

$J_{\text{air,sea}}$ . The exchange flux of CO<sub>2</sub> from the ocean to the atmosphere ( $J_{\text{air,sea}}$ ) is parameterized as:

$$F_{\text{gas}} = k_{\text{air,sea}} (C_i - (pC_i \times k_{\text{H}})), \quad (19)$$

where  $k_{\text{air,sea}}$  is the transfer coefficient,  $C_i$  and  $pC_i$  are the concentration of CO<sub>2</sub> in the ocean and the atmosphere, respectively, and  $k_{\text{H}}$  is Henry's constant for CO<sub>2</sub>.

$J_{\text{org,weath}}$ . The flux for the oxidative weathering of organic matter ( $J_{\text{org,weath}}$ ) was assumed to change with the amount of organic matter buried in the ocean:

$$J_{\text{org,weath}} = J_{\text{org,weath,mod}} \left( \frac{J_{\text{NPP}}}{J_{\text{NPP,mod}}} \right)^{\alpha_3}, \quad (20)$$

where  $J_{\text{org,weath,mod}}$  and  $J_{\text{NPP,mod}}$  denote the modern values for organic matter weathering and burial, and the coefficient  $\alpha_3$  denotes the strength of the response of organic matter weathering to the change in organic matter production by marine primary production, respectively.

$J_{\text{gyp}}$ . Similar to the previous parameterization, the flux of gypsum burial ( $J_{\text{gyp}}$ ) was parameterized as a function of the calcium and seawater sulfate concentration relative to the modern values for the flux of gypsum burial, calcium concentration and seawater sulfate concentration<sup>69,73</sup>:

$$J_{\text{gyp}} = J_{\text{gyp,mod}} \times \frac{[\text{Ca}^{2+}]}{[\text{Ca}^{2+}]_{\text{mod}}} \times \frac{[\text{SO}_4^{2-}]}{[\text{SO}_4^{2-}]_{\text{mod}}}. \quad (21)$$

Here  $J_{\text{gyp,mod}}$ ,  $[\text{Ca}^{2+}]$ ,  $[\text{Ca}^{2+}]_{\text{mod}}$ ,  $[\text{SO}_4^{2-}]$  and  $[\text{SO}_4^{2-}]_{\text{mod}}$  denote, respectively, the modern flux of gypsum burial, the calcium concentration, modern calcium concentration, seawater sulfate concentration and modern seawater sulfate concentration.

$J_{\text{pyr}}$ . Similar to previous studies, we consider the flux of pyrite burial ( $J_{\text{pyr}}$ ) to be a function of the modern maximum rate of microbial sulfate reduction, seawater sulfate concentration, the fraction of ocean anoxia and the concentration of reactive iron (that is,  $\text{Fe}^{2+}$ )<sup>31,34,69,73</sup>:

$$J_{\text{pyr}} = \text{area} \times f_{\text{anoxia}} \times \text{SRR}_{\text{max}} \times \frac{[\text{SO}_4^{2-}]}{[\text{SO}_4^{2-}] + K_{\text{SO}_4}} \times \frac{[\text{Fe}^{2+}]}{[\text{Fe}^{2+}] + K_{\text{Fe}}} \times \left( \frac{J_{\text{NPP}}}{J_{\text{NPP,mod}}} \right). \quad (22)$$

Here, area denotes the area of the ocean,  $f_{\text{anoxia}}$  is the fraction of ocean anoxia,  $\text{SRR}_{\text{max}}$  is the modern maximum sulfate reduction rate (when the rate of sulfate reduction is not limited by the amount of sulfate),  $[\text{SO}_4^{2-}]$  is as defined above,  $[\text{Fe}^{2+}]$  is the concentration of reactive iron, and  $K_{\text{SO}_4}$  and  $K_{\text{Fe}}$  are the half-saturation constants for microbial sulfate reduction and pyrite formation, respectively. Supplementary Table 1 contains the range of the values used in the model.

**Model calibration.** To explore the effect of anoxia and pyrite burial, we first calibrated the model to pre-industrial conditions. Specifically, we used the range of modelling parameters and fluxes reported for the modern Earth and solved the system of ordinary differential equations presented in ‘Global carbon and sulfur mass balance model’ in the Methods. The resulting model concentrations and fluxes were compared against those reported for a modern ocean–atmosphere system for the pre-industrial period. Our results from the calibration of the model exhibit a satisfactory consistency between the reported and modelled values of concentrations and fluxes (Supplementary Fig. 2).

### Sulfur isotope mass balance estimates of pyrite-driven alkalinity production

To estimate alkalinity fluxes from pyrite burial across the Phanerozoic eon (Fig. 1), we constructed a simple sulfur isotope mass balance model. We used a recent compilation of  $\delta^{34}\text{S}_{\text{sulfate}}$  ( $n = 9,225$ ) and  $\delta^{34}\text{S}_{\text{pyrite}}$  ( $n = 7,752$ ) data for the Phanerozoic eon<sup>65</sup>. We binned the data at 5 Myr intervals (Fig. 1a). On the basis of this sulfur isotope compilation, we calculated the proportion of sulfur buried as pyrite in marine sediments ( $f_{\text{pyr}}$ ) using the following equation:

$$f_{\text{pyr}} = (\partial_{\text{SW}} - \partial_{\text{input}})/\Delta, \quad (23)$$

where  $\partial_{\text{SW}}$  and  $\partial_{\text{input}}$  represent the isotopic composition of seawater sulfate and the riverine input flux, respectively. Modern  $\partial_{\text{input}}$  has been estimated at between 2 and 8‰, and we varied this parameter between these two end-members including a median of 5‰ (refs. 22,74–76). We computed  $\Delta$ , the isotopic difference between sulfate and sulfide, as the difference between the median  $\delta^{34}\text{S}_{\text{sulfate}}$  and  $\delta^{34}\text{S}_{\text{pyrite}}$  in each bin. For statistical reasons we only considered bins with at least ten coupled  $\delta^{34}\text{S}_{\text{sulfate}}$  and  $\delta^{34}\text{S}_{\text{pyrite}}$  measurements ( $n = 10$ ). Furthermore, we only considered  $f_{\text{pyr}}$  values between 0 and 1 as valid. For example, we discounted negative values for  $\Delta_{\text{seawater-pyrite}}$ , which arise when the median  $\delta^{34}\text{S}_{\text{pyrite}}$  composition is isotopically heavier than the median

$\delta^{34}\text{S}_{\text{sulfate}}$  composition in the same bin. Notably, this is particularly common during the Carboniferous period (–360–300 Ma) (Source Data Fig. 1). Whereas a mechanistic explanation for this observation is beyond the scope of the current work, it demonstrates an incomplete understanding of sulfur isotope systematics, which should be a target for future research<sup>14</sup>. The blue shading in (Fig. 1c) thus represents the upper and lower  $f_{\text{pyr}}$  values in each 5 Myr bin, based on the corresponding median  $\partial_{\text{SW}}$  and  $\Delta_{\text{seawater-pyrite}}$  values, computed over a range of  $\partial_{\text{input}}$ . Pyrite-associated alkalinity fluxes were obtained by multiplying the pyrite sulfur burial fluxes by a factor of two (equation (7)).

### Modelling LIP-OAEs

Estimates for the duration and global extent of ocean anoxia and for each of the LIP-OAEs studied were compiled from several key sources<sup>19,28,40,42,77</sup> and references therein, and are based on synthesized multi-proxy reconstructions (Supplementary Table 2). We note that estimates for the extent of anoxia during OAE1a (peak of ~10%) are based on recent uranium isotope records<sup>78</sup> that are not yet published but are assumed to be similar to OAE2<sup>28</sup>. Given the large uncertainties in both  $f_{\text{anoxia}}$  and total carbon emissions, we emphasize that the goal of the current study was not to reconstruct any particular LIP-OAE in detail but to provide a first-order framework for, and constraints on, possible anoxia–alkalinity feedback for a given carbon input strength across LIP-OAE multiple events. For example, dynamics in the severity of anoxia through time, in combination with other boundary conditions (for example, initial seawater sulfate and iron concentrations) have not been tuned for specific LIP-OAEs. However, our results do display general consistency with key environmental reconstructions based on available proxy evidence in terms of the relative magnitude and timing of environmental perturbations (Supplementary Fig. 1).

To calculate the carbon burden of individual LIPs we used a similar approach as presented in refs. 40,42. Briefly, we compiled estimates for the total volume of erupted basalt for each event ( $V$ )<sup>77</sup>. We then assumed a constant basalt density ( $\rho$ ) of 2.9 g cm<sup>–3</sup> (ref. 79). To estimate the maximum possible carbon release we assumed a melt  $\text{CO}_2$  concentration ( $w$ ) of between 0.7 and 2.5 wt%, which is taken as the upper value for most LIP magmas<sup>80–82</sup>, combined with 100% degassing efficiency. The total emitted carbon ( $T_C$ ) for each LIP was then calculated according to the following equation:

$$T_C = w \times V \times \rho. \quad (24)$$

We note that our lower estimates for total carbon degassing are of similar magnitude to published values (Supplementary Table 2). The larger estimates are slightly higher than published values. In this way, the corresponding modelled anoxia–alkalinity feedback strength can be considered to be a maximum estimate with respect to carbon input. Baseline model runs for each LIP event used the total carbon-release value, and this was assumed to have been emitted across both long and short degassing intervals (see below).

Generally, the maximum duration of LIP  $\text{CO}_2$  degassing for each event based on radio-isotopic dating analyses (for example, <sup>40</sup>Ar/<sup>39</sup>Ar, U–Pb) is greater than the duration of anoxia for the associated OAE (Supplementary Table 2). For example, age data for P–T event suggests that enhanced Siberian Trap volcanism could have lasted >10 Myr (refs. 40,42,83), with most estimates spanning on the order of 10–2,000 kyr (Supplementary Table 2). For example, geochemical proxy evidence suggests that associated P–T oceanic anoxia lasted on the order of ~100 kyr to 1 Myr (ref. 28). Owing to these contrasting timescales and large uncertainties, for each LIP-OAE we ran the model at both the upper and lower volcanic  $\text{CO}_2$  degassing rates: (1) the first scenario assumed that the total amount of carbon was released in a time frame equivalent to the duration of the OAE (yielding maximum degassing rates) and (2) the second scenario assumes that the total amount of carbon was released in a time frame equivalent to the LIP duration, as

determined by filtered robust age data<sup>40</sup> (yielding minimum degassing rates). For each model scenario, enhanced LIP volcanic carbon input followed a gaussian distribution and the anoxia–alkalinity feedback was active for the duration of the model run. For both upper and lower degassing scenarios, the extent of oceanic anoxia was held constant, and the average value was used, which is generally on the lower end (conservative) of the range of reconstructed values (Source Data Fig. 2). For example, for the P–T LIP-OAE, the strength of the anoxia–alkalinity feedback at 14% oceanic anoxia ( $f_{\text{anoxia}}$ ) was tested for both long (1 Myr) and short (100 kyr) Siberian Trap volcanic degassing scenarios (Supplementary Fig. 3). For all modelled scenarios, the impacts of oceanic anoxia and pyrite-burial-based alkalinity production fluxes are reported as the difference ( $\Delta$ ) between model runs with and without the pyrite-burial-driven alkalinity feedback (that is, with and without expanded oceanic anoxia relative to modern).

**LOSCAR simulations.** To build confidence in our model we performed comparative carbon cycle perturbation simulations using the established LOSCAR (Long-term Ocean–atmosphere–Sediment CARbon cycle Reservoir) model<sup>68</sup>. We used the pre-industrial configuration of LOSCAR, which has similar boundary conditions as our model (Supplementary Fig. 2). We simulated the same carbon-release scenarios for each of the five LIP-OAEs (Supplementary Fig. 3), starting from model time zero, with the run lasting 10 Myr. LOSCAR lacks the anoxia–alkalinity feedback, and thus peak model results ( $p_{\text{CO}_2}$ , pH) were compared with the baseline outputs from our model, also without the feedback (Supplementary Fig. 4). All model results show strong agreement and overlap within 1SD (Source Data Supplementary Data 1).

## Data availability

All data and model information are available in the article and its Supplementary Information. Source data are provided with this paper. These data are available via the OSF repository at <https://doi.org/10.17605/OSF.IO/X5RF8> (ref. 84).

## Code availability

The computer code for the current study is available via Zenodo at <https://doi.org/10.5281/zenodo.14889587> (ref. 85).

## References

- Zeebe, R. E. & Wolf-Gladrow, D. *CO<sub>2</sub> in Seawater: Equilibrium, Kinetics, Isotopes* (Elsevier, 2001).
- Zeebe, R. E. LOSCAR: Long-term Ocean-atmosphere-Sediment CARbon cycle Reservoir Model v2.0.4. *Geosci. Model Dev.* **5**, 149–166 (2012).
- Ozaki, K., Reinhard, C. T. & Tajika, E. A sluggish mid-Proterozoic biosphere and its effect on Earth's redox balance. *Geobiology* **17**, 3–11 (2019).
- Laakso, T. A. & Schrag, D. P. A small marine biosphere in the Proterozoic. *Geobiology* **17**, 161–171 (2019).
- Katsev, S. & Crowe, S. A. Organic carbon burial efficiencies in sediments: the power law of mineralization revisited. *Geology* **43**, 607–610 (2015).
- Fakhraee, M., Planavsky, N. J. & Reinhard, C. T. The role of environmental factors in the long-term evolution of the marine biological pump. *Nat. Geosci.* **13**, 812–816 (2020).
- Bergman, N. M., Lenton, T. M. & Watson, A. J. COPSE: a new model of biogeochemical cycling over Phanerozoic time. *Am. J. Sci.* **304**, 397–437 (2004).
- Fike, D. A. & Grotzinger, J. P. A paired sulfate–pyrite  $\delta^{34}\text{S}$  approach to understanding the evolution of the Ediacaran–Cambrian sulfur cycle. *Geochim. Cosmochim. Acta* **72**, 2636–2648 (2008).
- Ivanov, M. V., Grinenko, V. A. & Rabinovich, A. P. in *The Global Biogeochemical Sulphur Cycle* (eds Ivanov, M. V. & Freney, J. R.) 297–356 (Wiley, 1983).
- Canfield, D. E. The evolution of the Earth surface sulfur reservoir. *Am. J. Sci.* **304**, 839–861 (2004).
- Mills, B., Daines, S. J. & Lenton, T. M. Changing tectonic controls on the long-term carbon cycle from Mesozoic to present. *Geochem. Geophys. Geosyst.* **15**, 4866–4884 (2014).
- Percival, L. et al. Uranium-isotope records of global ocean deoxygenation during the Early Aptian Oceanic Anoxic Event (OAE 1a). In *Goldschmidt Abstracts 2023* <https://doi.org/10.7185/gold2023.17582> (European Association of Geochemistry, Geochemical Society, 2023).
- Moore, J. G. Density of basalt core from Hilo drill hole, Hawaii. *J. Volcanol. Geotherm. Res.* **112**, 221–230 (2001).
- Black, B. A., Karlstrom, L. & Mather, T. A. The life cycle of large igneous provinces. *Nat. Rev. Earth Environ.* **2**, 840–857 (2021).
- Black, B. A. & Gibson, S. A. Deep carbon and the life cycle of large igneous provinces. *Elements* **15**, 319–324 (2019).
- Lowenstern, J. B. Carbon dioxide in magmas and implications for hydrothermal systems. *Miner. Depos.* **36**, 490–502 (2001).
- Ivanov, A. V. et al. Siberian Traps large igneous province: evidence for two flood basalt pulses around the Permo-Triassic boundary and in the Middle Triassic, and contemporaneous granitic magmatism. *Earth Sci. Rev.* **122**, 58–76 (2013).
- Bauer, K. Climate stabilization by alkalinity production from pyrite burial during oceanic anoxia. *Open Science Framework* <https://doi.org/10.17605/OSF.IO/X5RF8> (2025).
- MjFakh. MjFakh/C\_S-box-model: C\_S Box Model\_1.0. *Zenodo* <https://doi.org/10.5281/zenodo.14889587> (2025).

## Acknowledgements

Funding was provided through an NSERC discovery grant (awarded to S.A.C.). M.F., N.J.P. and C.T.R. acknowledge funding from the NASA Interdisciplinary Consortia for Astrobiology Research (ICAR program). We thank A. Mucci and W. Fischer who provided suggestions.

## Author contributions

Funding acquisition: S.A.C., M.F., N.J.P. and C.T.R. Conceptualization: M.F., K.W.B., S.A.C., N.J.P. and C.T.R. Methodology: K.W.B. and M.F. Investigation: K.W.B. and M.F. Visualization: K.W.B. and M.F. Writing (original draft): K.W.B., S.A.C. and M.F. Writing (review and editing): all authors.

## Competing interests

The authors declare no competing interests.

## Additional information

**Supplementary information** The online version contains supplementary material available at <https://doi.org/10.1038/s41561-025-01698-0>.

**Correspondence and requests for materials** should be addressed to Mojtaba Fakhraee, Kohen W. Bauer or Sean A. Crowe.

**Peer review information** *Nature Geoscience* thanks the anonymous reviewers for their contribution to the peer review of this work. Primary Handling Editor: Stefan Lachowycz, in collaboration with the *Nature Geoscience* team.

**Reprints and permissions information** is available at [www.nature.com/reprints](http://www.nature.com/reprints).